PHYSICAL REVIEW B **95**, 045207 (2017)

Overtones of interlayer shear modes in the phonon-assisted emission spectrum of hexagonal boron nitride

T. Q. P. Vuong,[1] G. Cassabois,[1,*] P. Valvin,[1] V. Jacques,[1] R. Cuscó,[2] L. Artús,[2] and B. Gil[1]
[1]*Laboratoire Charles Coulomb, UMR 5221 CNRS-Université de Montpellier, 34095 Montpellier, France*
[2]*Institut Jaume Almera, Consejo Superior de Investigaciones Cientficas (ICTJA-CSIC), 08028 Barcelona, Spain*
(Received 20 October 2016; revised manuscript received 3 January 2017; published 17 January 2017)

We address the intrinsic optical properties of hexagonal boron nitride in deep ultraviolet. We show that the fine structure of the phonon replicas arises from overtones involving up to six low-energy interlayer shear modes. These lattice vibrations are specific to layered compounds since they correspond to the shear rigid motion between adjacent layers, with a characteristic energy of about 6–7 meV. We obtain a quantitative interpretation of the multiplet observed in each phonon replica under the assumption of a cumulative Gaussian broadening as a function of the overtone index, and with a phenomenological line broadening taken identical for all phonon types. We show from our quantitative interpretation of the full emission spectrum above 5.7 eV that the energy of the involved phonon mode is 6.8 ± 0.5 meV, in excellent agreement with temperature-dependent Raman measurements of the low-energy interlayer shear mode in hexagonal boron nitride. We highlight the unusual properties of this material where the optical response is tailored by the phonon group velocities in the middle of the Brillouin zone.

DOI: 10.1103/PhysRevB.95.045207

I. INTRODUCTION

Boron nitride allotropes are characterized by a great diversity of forms comparable to the one found in the carbon family [1]. Cubic boron nitride (cBN) crystallizes in the zinc-blende lattice so that diamond and cBN are isostructural, sharing many properties like a large band gap (>5 eV), high thermal conductivity, chemical inertness, and hardness. The sp^3 hybridization of the atomic orbitals in these materials contrasts with the sp^2 one specific to graphite and hexagonal boron nitride (hBN), also called "white" graphite. With the same honeycomb structure inside a monolayer, graphite and hBN are lamellar compounds which are however not strictly isostructural. The stacking along the c axis is Bernal (so called AB) in graphite, and AA′ in hBN, one boron atom sitting exactly above one nitrogen atom from one layer to another. Graphite and hBN also share many physical properties such as high thermal and chemical stabilities, and offer the possibility to be easily exfoliated in monolayers for Van der Waals heterostructures [2], or to exist in rolled sheets in the form of nanotubes [3]. However, a dramatic difference between "white" and "black" graphites is their electronic band structure.

Graphite is a gapless compound with conduction and valence bands having extrema at the K points of the Brillouin zone, whereas hBN is a wide band-gap material (∼6 eV [4]) with an indirect configuration of very peculiar nature since the conduction band minimum sits at the M point while the valence band maximum is around the K point of the Brillouin zone. This is a major difference with cubic semiconductors where the valence band maximum is located at the zone center (Γ point), as in diamond, silicon, germanium etc.... The very important consequence is that phonon-assisted recombination in hBN involves phonons in the middle of the Brillouin zone (around T points, as sketched in the inset of Fig. 2) instead of phonons from the same valley as for the conduction band minimum in indirect cubic semiconductors. This original phenomenology in hBN results in an optical response involving phonons with a finite group velocity, leading to phonon replicas displaying sharp resonances [4] instead of the standard broad bands expected from the mapping of the excitonic quasicontinuum in phonon-assisted optical processes [5].

Albeit the intrinsic optical response in hBN in the deep ultraviolet is fully determined by phonons in the middle of the Brillouin zone, it was also demonstrated that intervalley scattering occurs in hBN, with the emission of zone-edge transverse optical phonons at the K point [6]. Thanks to the presence of structural defects leading to a density of final electronic states, the efficiency of higher-order processes becomes large enough to be observable, in particular intervalley scattering assisted by transverse optical phonons in K points. Still, surprisingly, no evidence for the implication of zone-center phonons has been demonstrated so far in the intrinsic optoelectronic properties of hBN.

In this paper we show that the fine structure of the phonon replicas in hBN arises from overtones involving up to six low-energy Raman-active phonons, at the zone center. These lattice vibrations are specific to layered compounds since they correspond to the shear rigid motion between adjacent layers, with a characteristic energy of about 6–7 meV. We obtain a quantitative interpretation of the multiplet observed in each phonon replica under the assumption of a cumulative broadening as a function of the overtone index and with a phenomenological line broadening taken identical for all phonon types. We point out that the excellent agreement between our theoretical model and the emission spectrum is reached with the phonon group velocity as the only varying physical parameter from one phonon replica to another. We further discriminate between Gaussian and Lorentzian line profiles and discuss it in the context of phonon-assisted broadening. Finally, we show from our quantitative interpretation that the energy of the involved phonon mode is 6.8 ± 0.5 meV, in excellent agreement with temperature-dependent Raman

*guillaume.cassabois@umontpellier.fr

measurements of the low-energy interlayer shear mode in hBN.

II. PHOTOLUMINESCENCE SPECTROSCOPY

A. Experiments

Our experiments consist of photoluminescence (PL) spectroscopy in bulk hBN. Our sample is a commercial hBN crystal from HQ Graphene. In our experimental setup, the sample is held on the cold finger of a closed-cycle cryostat for temperature-dependent measurements from 10 K to room temperature. We perform two-photon excitation spectroscopy, and the excitation beam is provided by the second harmonic of a Ti:Sa oscillator, tuned at 408 nm in resonance with the sharp peak in the two-photon excitation spectrum [4]. The spot diameter is of the order of 100 μm, with a power of 50 mW. An achromatic optical system couples the emitted signal to our detection system, composed of a $f = 500$ mm Czerny-Turner monochromator, equipped with a 1800 grooves/mm grating blazed at 250 nm, and with a back-illuminated charge-coupled device (CCD) camera (Andor Newton 920), with a quantum efficiency of 50% at 210 nm. The integration time is of 15 s. We use a band-pass filter around 200 nm with a low transmission at 400 nm in front of the spectrometer for complete laser stray light rejection.

B. Results

In Fig. 1, we display the PL spectrum of bulk hBN above 5.7 eV (below 218 nm), at 10 K. In this spectral region, the PL signal corresponds to the intrinsic phonon-assisted emission with five phonon replicas having maxima at 5.76, 5.79, 5.86, 5.89, and 5.93 eV. These lines display an energy spacing exactly matching the splitting of the different phonon

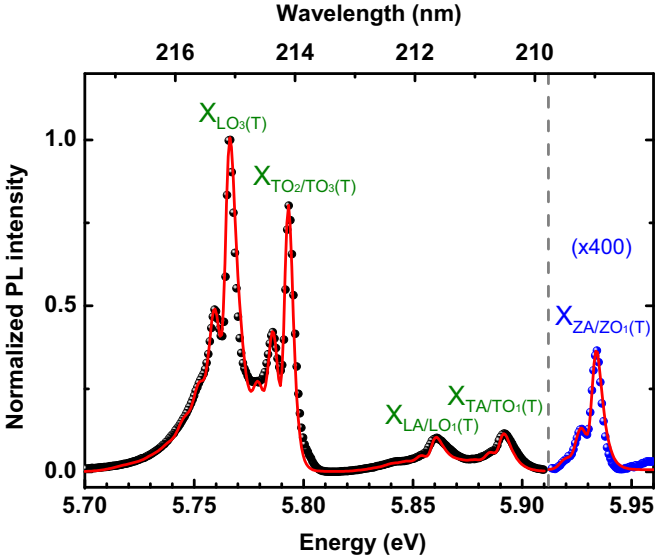

FIG. 1. Photoluminescence spectrum in bulk hBN in the deep ultraviolet under two-photon excitation at 3.03 eV, at 10 K. Experimental data (symbols), theoretical fit (red line). X_μ stands for the replica involving the phonon mode μ in the middle of the Brillouin zone around T points.

TABLE I. The columns indicate the energy of the PL line, the corresponding energy detuning with the indirect exciton iX (evaluated in Ref. [4]), the phonon energy at T points calculated in Ref. [8], the corresponding phonon type, and the group velocity v_g at T points calculated in Ref. [8].

Line (eV)	Detuning (meV)	Calculated phonon energy (meV)	Phonon type (μ)	Group velocity v_g (10^4 m s^{-1})
5.93	22	20/21.7	ZA/ZO$_1$(T)	0.43
5.89	64	64.6/65.1	TA/TO$_1$(T)	1.1
5.86	95	94.4/94.3	LA/LO$_1$(T)	1.3
5.79	162	162.6/162.7	TO$_2$/TO$_3$(T)	0.18
5.76	188	185.4	LO$_3$(T)	0.57

branches in the middle of the Brillouin zone (around T points) since radiative recombination in hBN must be assisted by the emission of phonons of wave-vector **MK** in order to fulfill momentum conservation [4,6].

In Refs. [4,6], the five phonon replicas at 5.76, 5.79, 5.86, 5.89, and 5.93 eV had been labeled LO, TO, LA, TA, and ZA, respectively, following the study of the vibrational properties in hBN reported in Ref. [7]. The more detailed study of the hBN phonon dispersion performed in Ref. [8] calls for a more precise labeling of the phonon replicas. Since several optical and acoustic phonon branches lying very close in energy occur in the phonon dispersion, both phonon types can be in principle involved in the phonon-assisted recombination processes. A consistent labeling scheme for all longitudinal and transverse optical phonons is given in Ref. [8].

On the basis of Ref. [8], we provide in Table I an updated labeling of the phonon replicas. For each line, we display the energy of the phonon replica in the PL spectrum, the corresponding energy detuning with the indirect exciton iX (evaluated in Ref. [4]), the phonon energy at T points calculated in Ref. [8], the corresponding phonon type (the latter giving the subscript of the phonon replicas, as shown in Fig. 1), and the group velocity v_g at T points calculated in Ref. [8]. Note that, in Fig. 1, the signal intensity of the $X_{ZA/ZO_1(T)}$ phonon replica is the smallest one because of the selection rules controlling radiative recombination assisted by phonon emission in hBN. Indeed, the ZA/ZO$_1$ phonon replica is forbidden by symmetry in our experimental geometry, where the emission wave vector is parallel to the c axis [4,9].

Besides the varying magnitude of the different lines, we nevertheless observe the same multiplet structure for each phonon replica. We see a sharp and intense line of full width at half maximum (FWHM) of about 4 meV and secondary maxima of lower intensity, red-shifted by approximately 7 meV. The visibility of the fine structure is the largest for the phonon replicas at 5.76 and 5.79 eV while hardly observable for the other ones, except for $X_{ZA/ZO_1(T)}$. We will see below that it is directly related to the group velocity of the phonon modes, which is taken into account in our theoretical fit displayed by solid line in Fig. 1, showing a fair agreement with our experimental data and providing the first quantitative interpretation of the fine structure of the phonon replicas, as detailed below.

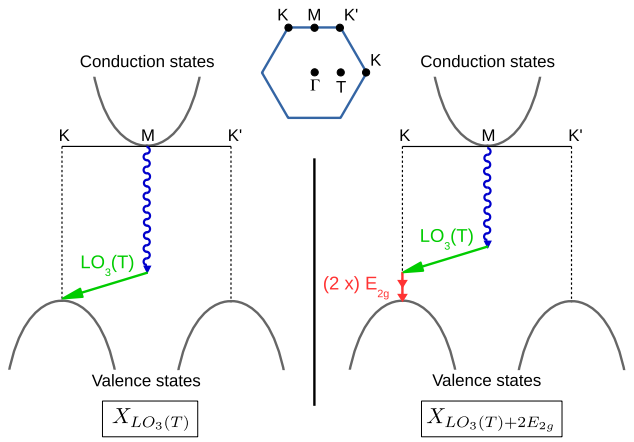

FIG. 2. Schematic representations, in the single-particle picture of the electronic band structure, of the phonon-assisted recombination processes of the $X_{LO_3(T)}$ line (left part), and of the $X_{LO_3(T)+2E_{2g}}$ one (right part). Inset: top view of the first Brillouin zone with high symmetry points. The green arrows correspond to the $LO_3(T)$ phonon in the middle of the Brillouin zone, and the red arrows to the low-energy interlayer shear phonons of E_{2g} symmetry.

C. Interpretation of the fine structure of the phonon replicas

We present in this section our theoretical model describing the fine structure, and more generally the whole line profile of the phonon replicas. Our interpretation is based on the existence of phonon replicas associated with phonon overtones involving up to six low-energy zone-center phonons in addition to the phonon at the T point. While the latter is required for momentum conservation in the phonon-assisted recombination process in hBN (Fig. 2, left), the formers are on the contrary zone-center phonons which do not modify the momentum balance, and which can thus contribute in high-order processes (Fig. 2, right). These low-energy Raman-active phonons of E_{2g} symmetry are specific to layered compounds since they correspond to the shear rigid motion between adjacent layers, with a characteristic energy of about 6–7 meV [8].

More specifically, our model relies on the superposition of phonon-assisted emission lines $X_{\mu+nE_{2g}}$ with $n \leqslant 6$, where one photon is emitted together with the emission of one phonon μ in the middle of the Brillouin zone [with $\mu = LO_3(T)$, or $TO_2/TO_3(T)$, or $LA/LO_1(T)$, or $TA/TO_1(T)$, or $ZA/ZO_1(T)$] and n interlayer shear phonons E_{2g} of energy Δ.

We first discuss the emission spectrum $H_{\mu,n}(E)$ for a given line $X_{\mu+nE_{2g}}$. Under the assumption of a full thermal equilibrium and nondegenerate conditions (the exciton distribution can be well approximated by a Boltzmann distribution with a temperature $\mathcal{T}$), the relationship between the transition probabilities of emission (W_{em}) and absorption (W_{abs}) *at the same energy* can be quantitatively expressed as $W_{em}(E) \propto W_{abs}(E)\exp(-E/k_B\mathcal{T})$ [10,11]. Recombination assisted by phonon emission being the inverse process of photon absorption assisted by phonon absorption, the emission spectrum $H_{\mu,n}(E)$ is given by:

$$H_{\mu,n}(E) = \rho(E-\delta_{\mu,n})f_\mu(E-\delta_{\mu,n})e^{-\frac{E-\delta_{\mu,n}}{k_B\mathcal{T}}} \qquad (1)$$

where $\delta_{\mu,n} = E_{iX} - E_\mu - n\Delta$ (with E_{iX} the indirect exciton energy), ρ is the joint density of states [5], and f_μ the function describing the wave-vector dependence of the electron-phonon matrix element which is calculated in the Supplemental Material of Ref. [4]. Note that in Ref. [4], we were interested in the absorption assisted by phonon emission occurring at the mirror energy $E_{iX} + E_\mu + n\Delta$, which has the same spectral dependence as the absorption assisted by phonon absorption but occurring at $E_{iX} - E_\mu - n\Delta$ [5,12].

The joint density of states ρ is given by:

$$\rho(x) = \Theta(x)\left(\frac{2M_n}{\hbar^2}\right)^{\frac{3}{2}}\sqrt{x} \qquad (2)$$

with x an energy, Θ the step function, and M_n the excitonic effective mass [5]. The function f_μ describing the wave-vector dependence of the electron-phonon matrix element is given by [4]:

$$f_\mu(x) = \frac{1}{\left(4 + a^2\left(k_T + \frac{x}{\hbar v_g^\mu}\right)^2\right)^4} \qquad (3)$$

with a the excitonic Bohr radius, k_T the phonon wave vector in the middle of the Brillouin zone, and v_g^μ the group velocity of the μ phonon branch around T points.

We further stress that the joint density of states ρ is identical for all phonon replicas, whereas the f_μ function depends on the phonon nature through the group velocity v_g^μ, thus accounting for the cutoff of the exciton-phonon matrix element for wave vectors higher than $1/a$. As a matter of fact, the lower v_g^μ the larger the energy variation of the exciton-phonon matrix element. This effect is at the heart of the varying visibility of the fine structure of the replicas as a function of the phonon type, v_g^μ being the only varying quantity from one type of replica to another in the theoretical fit displayed in Fig. 1.

For the sake of clarity, we proceed below by increasing complexity by considering:

(1) case (i) displayed in Fig. 3(a): no additional broadening compared to the analytical expression given by Eq. (1) for the phonon-assisted emission spectrum,

(2) case (ii) displayed in Fig. 3(b): a fixed Gaussian broadening independent of the index n of the overtone,

(3) case (iii) displayed in Fig. 3(c): a Gaussian cumulative broadening which corresponds to the fit displayed in Fig. 1,

(4) case (iv) displayed in Fig. 3(d): a Lorentzian cumulative broadening for comparison.

For all the calculated profiles displayed in Fig. 3, we take $a = 3$ Å [4], $k_T = \Gamma K/2 = 0.87\ 10^{-10}$ m^{-1}, and $v_g^\mu = 0.43$, 1.1, 1.3, 0.18, 0.57 in units of 10^4 m.s^{-1} for $\mu = ZA/ZO_1(T)$, $TA/TO_1(T)$, $LA/LO_1(T)$, $TO_2/TO_3(T)$, and $LO_3(T)$, respectively, which correspond to the calculated values of the phonon group velocity in the middle of the Brillouin zone in Ref. [8], also displayed in Table I. For the Boltzmann distribution in Eq.(1), we take for $\mathcal{T}$ an effective electronic temperature of 50 K, following our analysis of the incomplete thermalization of the excitonic gas with the lattice at a sample temperature of 10 K [4].

Note that, in Fig. 3, we only display the PL spectrum of the $X_{LO_3(T)}$ and $X_{TO_2/TO_3(T)}$ phonon replicas (spanning the 5.72–5.82 eV spectral domain) where the high visibility of the

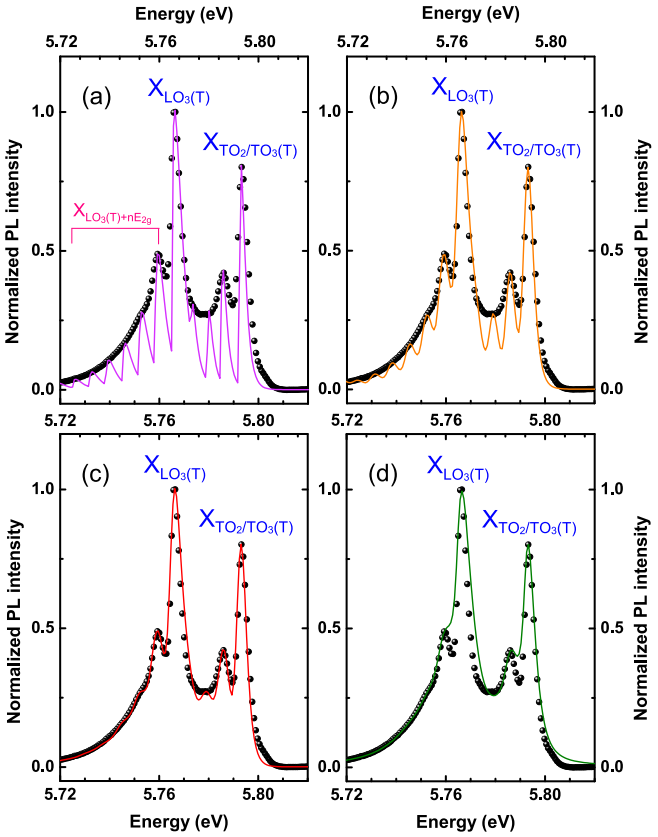

FIG. 3. Experimental data (symbols) and fit (solid line) of the phonon-assisted emission spectrum in hBN: (a) without any line-broadening, (b) with a Gaussian broadening identical for each overtone, (c) with a Gaussian cumulative broadening (corresponding to Fig. 1), and (d) with a Lorentzian cumulative broadening. The energy Δ of the Raman-active phonons E_{2g} is 6.8 meV. The amplitudes A_n^μ of the different components used in the fits are displayed in Fig. 4.

fine structure allows a detailed insight into the four different cases mentioned above.

1. Case (i): No broadening

In case (i), the PL spectrum of the phonon replicas reads:

$$I(E) = \sum_{\mu} \sum_{n=0}^{N_{E_{2g}}^{\mu}} A_n^{\mu} H_{\mu,n}(E) \tag{4}$$

where A_n^μ is a fitting parameter corresponding to the amplitude of the $H_{\mu,n}(E)$ line, and $N_{E_{2g}}^{\mu}$ is the number of interlayer shear phonons considered in the fit. The pink solid line in Fig. 3(a) is obtained with $N_{E_{2g}}^{LO_3(T)} = 6$ and $N_{E_{2g}}^{TO_2/TO_3(T)} = 3$. The smaller $N_{E_{2g}}^{TO_2/TO_3(T)}$ value comes from the overlap of the low-energy tail of the TO_2/TO_3 phonon replica with the high-energy one of the LO_3 phonon replica, making the estimation of $A_n^{TO_2/TO_3(T)}$ irrelevant for $n > 3$.

In this approximation, the calculated PL spectrum consists in a comb of asymmetric lines, providing an overall poor agreement with the experimental data. Each component reflects the general features of the $H_{\mu,n}(E)$ spectrum, i.e., a steep increase on the low energy side which is reminiscent of the abrupt rise of the joint density of states ρ [Eq. (2)], and a smoother decrease on the high energy side due to the reduction of the electron-phonon matrix element described by the f_μ function [Eq. (3)]. The larger the group velocity v_g^μ, the smoother the f_μ decrease, and thus the broader the $H_{\mu,n}(E)$ line, as observed in Fig. 3(a) where the $H_{\mu,n}(E)$ components are broader for LO_3 phonons which have a larger group velocity than TO_2/TO_3 phonons (Table I).

In Fig. 3(a), the A_n^μ amplitudes are chosen in order to reproduce the envelope given by the spectrum of the LO_3 and TO_2/TO_3 phonon replicas, but major discrepancies remain. Most importantly, the $H_{\mu,n}(E)$ components are too sharp, even in the case $n = 0$, where the $H_{\mu,0}(E)$ linewidth is smaller than the 4 meV-FWHM of the narrowest lines at 5.765 and 5.795 eV.

2. Case (ii): Constant Gaussian broadening

In case (ii), we consider a fixed Gaussian broadening independent of the index n of the overtone. Consequently, after convolution of the emission spectrum of case (i) [Eq. (4)] with a Gaussian function, the theoretical emission spectrum reads:

$$I(E) = \left(\sum_{\mu} \sum_{n=0}^{N_{E_{2g}}^{\mu}} A_n^{\mu} H_{\mu,n}(E) \right) \otimes G_0(E), \tag{5}$$

where the Gaussian function $G_0(E)$ is given by:

$$G_0(E) = \exp\left(-\frac{E^2}{\sigma_0^2}\right). \tag{6}$$

The orange solid line in Fig. 3(b) is calculated with the same amplitudes A_n^μ as in Fig. 3(a) and with $\sigma_0 = 2$ meV. Such a value leads to a FWHM $2\sqrt{ln2}\sigma_0$ of $G_0(E)$ of 3.3 meV, which is close to the 4.2 meV-FWHM of the narrowest line at 5.795 eV. In fact, σ_0 was chosen in order to reach a good agreement with this sharp line, corresponding to $n = 0$ where no interlayer shear phonon is emitted.

The present version of our model better fits our data than in case (i). In particular, we correctly account for the prominent doublet structure of the LO_3 and TO_2/TO_3 phonon replicas, although the first overtone appears too sharp again for the TO_2/TO_3 phonon replica. Moreover, we still observe a poor agreement for the low-energy sides of the LO_3 and TO_2/TO_3 phonon replicas, i.e., for the overtones of interlayer shear modes $n \geqslant 2$.

3. Case (iii): Cumulative Gaussian broadening

The red solid line in Fig. 3(c) is the calculated fit in case (iii), where we assume a Gaussian cumulative broadening. This means that each term $H_{\mu,n}(E)$ of order n is convoluted with a given Gaussian function $G_n(E)$ independently of the phonon nature μ, so that the calculated PL spectrum of the phonon replicas displayed in Fig. 3(c) reads:

$$I(E) = \sum_{\mu} \sum_{n=0}^{N_{E_{2g}}^{\mu}} A_n^{\mu} H_{\mu,n}(E) \otimes G_n(E), \tag{7}$$

where the Gaussian function $G_n(E)$ is given by:

$$G_n(E) = \exp\left(-\frac{E^2}{\sigma_n^2}\right) \quad (8)$$

with $\sigma_n^2=(n+1)\sigma_0^2$ and $\sigma_0 = 2$ meV. Such an expression for σ_n consists of making the assumption of a cumulative Gaussian broadening, the convolution of two Gaussian functions of width σ_a and σ_b having a width $\sqrt{\sigma_a^2+\sigma_b^2}$. From a physical point of view, in the case of independent broadening processes, the total linewidth is obtained, in the Gaussian broadening limit, by adding each linewidth squared and then taking the square root of the sum.

Case (iii) of our model provides an excellent agreement with our data, as seen in Fig. 3(c) and in Fig. 1 for the whole emission spectrum. Note that our fitting procedure fairly reproduces fine details of the PL spectrum, such as the shoulder at 5.75 eV arising from $X_{LO_3(T)+2E_{2g}}$ [Figs. 3(a) and 3(c)].

In our specific case, the consideration of a cumulative broadening means that the linewidth of each $H_{\mu,n}(E)$ component increases with the index n of the overtone. This assumption stems from the general phenomenology observed in experiments [13,14], and predicted by theory [15], of an increasing broadening of phonon replicas with the overtone index. The presence of this effect in the phonon-assisted emission spectrum in hBN indicates that the linewidth of the different $X_{\mu+nE_{2g}}$ components is limited by phonon-assisted broadening, which increases as a function of the order of the electron-phonon interaction process. This important point will be further discussed below, in the light of the additional comparison of the Gaussian versus Lorentzian broadening type.

We stress again that the assumption of cumulative broadening [$\sigma_n^2 = (n+1)\sigma_0^2$, with $\sigma_0 = 2$ meV] does not depend on the phonon type μ. This key point further highlights the fact that the differences observed in the various LO_3, TO_2/TO_3, LA/LO_1, TA/TO_1, and ZA/ZO_1 phonon replicas in Fig. 1 only come from the variations of the group velocity v_g^μ from one type of phonon to another (Table I). This fundamental aspect brings a considerable strength to our approach, thus validating our quantitative interpretation of the emission spectrum in hBN in the deep ultraviolet, and also pointing out the originality of this material where the optical response is controlled by the phonon group velocities in the middle of the Brillouin zone.

In Fig. 4, we display the amplitudes A_n^μ of the different components $X_{\mu+nE_{2g}}$ of the phonon-assisted emission spectrum, used in the fit displayed in Fig. 1 [and Fig. 3(c)]. For each phonon replica, we have taken $N_{E_{2g}}^\mu = 6, 5, 4, 3, 2$ for $\mu = LO_3(T), LA/LO_1(T), TA/TO_1(T), TO_2/TO_3(T)$, and $ZA/ZO_1(T)$, respectively, the latter values being smaller than for longitudinal phonons because of the overlap with the high-energy tail of the neighboring lines, as already discussed above. In Fig. 4 plotted on a semilog scale, we observe an exponential decrease of A_n^μ as a function of the overtone index n whatever the phonon nature μ. As expected, the higher the order of the electron-phonon interaction process, the smaller its probability. A quantitative interpretation of the decrease of A_n^μ with n would give a direct insight into the physics of the electron-phonon coupling in hBN. This study is beyond the scope of this paper since it requires a full calculation of the indirect exciton wave function in hBN complemented by the inclusion of the electron-phonon interaction. Such a program is at the frontier of state-of-the-art *ab initio* calculations, which still do not include both electron-hole and electron-phonon couplings, and are also limited to low-order processes in the latter case [16].

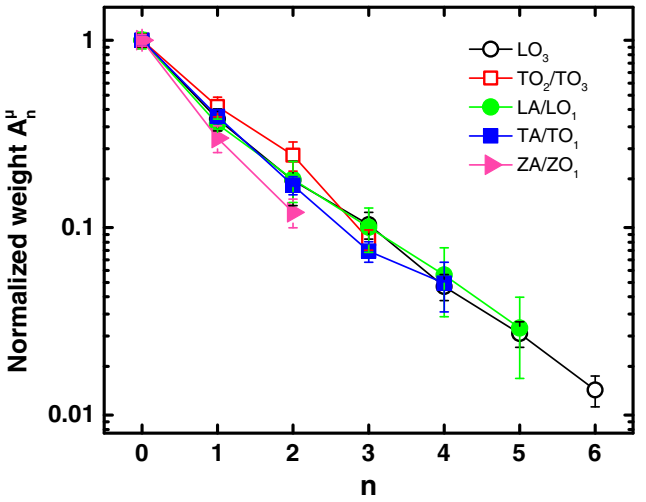

FIG. 4. Normalized weight A_n^μ of the overtones of interlayer shear modes used in Fig. 1, as a function of overtone index n, for each type of phonon replicas: ZA/ZO_1 (filled triangle), TA/TO_1 (filled square), LA/LO_1 (filled circle), TO_2/TO_3 (open square), LO_3 (open circle).

4. *Case (iv): Cumulative Lorentzian broadening*

The green solid line in Fig. 3(d) corresponds to case (iv) where we consider a cumulative broadening but for Lorentzian lines. The PL spectrum of the phonon replicas displayed in Fig. 3(d) thus reads:

$$I(E) = \sum_\mu \sum_{n=0}^{N_{E_{2g}}^\mu} A_n^\mu H_{\mu,n}(E) \otimes L_n(E), \quad (9)$$

where the Lorentzian function $L_n(E)$ is given by:

$$L_n(E) = \frac{(\Gamma_n/2)^2}{E^2 + (\Gamma_n/2)^2} \quad (10)$$

with $\Gamma_n = (n+1)\Gamma_0$ and $\Gamma_0 = 3.3$ meV. In contrast to case (iii), one has to take the linear superposition of the linewidths, in the Lorentzian broadening limit. Such a value for Γ_0 ensures that the Lorentzian function $L_0(E)$ has the same FWHM as the Gaussian function $G_0(E)$ with $\sigma_0 = 2$ meV, in order to keep a good agreement with the narrow lines at 5.765 and 5.795 eV [Fig. 3(d)], corresponding to $n = 0$ where no interlayer shear phonon is emitted.

Nevertheless, we observe a global degradation of the data fitting because of the slow decay of Lorentzian wings. In particular, we see that the prominent doublet structure of the X_μ and $X_{\mu+E_{2g}}$ lines is completely lost in the case of a Lorentzian broadening. Even if the assumption of cumulative broadening leads again to a good fit on the low-energy side of the LO_3 phonon replica [Fig. 3(d)], the poorer agreement reached in case (iv) compared to case (iii) allows us to discriminate between Lorentzian and Gaussian broadening,

and we conclude that the phonon-assisted broadening could surprisingly be in the Gaussian limit in hBN, as further discussed below.

D. Phonon-assisted broadening in the Gaussian limit

The optical response of solid-state systems is affected by two kinds of broadening, which are described in terms of homogeneous and inhomogeneous broadenings. The latter one comes from disorder, extended or point defects, and more generally any inhomogeneity in the sample structure. As far as homogeneous broadening is concerned, its major sources in semiconductors are carrier-carrier interactions, electron-phonon coupling, and spectral diffusion. Homogeneous broadening is usually considered to be characterized by a Lorentzian line profile, whereas inhomogeneous broadening by more complex distribution functions, the most generic one being the Gaussian statistics. However, even in the case of a purely homogeneously-broadened system, the line profile is not necessarily a Lorentzian function.

A specific example in the context of spectral diffusion is the smooth Lorentzian-Gaussian transition observed in the emission spectrum of a single quantum dot [17]. Within the general framework developed in the seminal paper of Kubo [18], a Gaussian spectrum corresponds to the so-called slow modulation limit where the product of the spectral fluctuation amplitude and fluctuation correlation time is larger than one. On the contrary, when this figure of merit is smaller than one, motional narrowing occurs and the optical response takes a Lorentzian profile, with the historical textbook example of nuclear magnetic resonance.

In fact, the same phenomenology applies to the phonon-assisted broadening, as discussed by Toyozawa in Ref. [19]. In his general theory of the lineshapes of the exciton absorption bands, Toyozawa demonstrated that, when the exciton-lattice coupling is weak, the absorption band is of a Lorentzian shape, whereas, if the coupling is strong, the absorption band is expected to be of a Gaussian shape, with the same underlying physics as for spectral diffusion. We thus conclude that the Gaussian broadening leading to the best description of the emission spectrum in hBN [Figs. 3(c) and 3(d)] can be of homogeneous nature as the result of an intrinsic interaction process, namely the electron-phonon coupling in hBN.

The intrinsic origin of the Gaussian broadening revealed in Fig. 3 is strongly supported by the systematic observation of the same emission spectrum above 5.7 eV in hBN, as illustrated for instance by Ref. [20] where nearly identical emission spectra are reported in samples fabricated in four different growth facilities. Moreover, as discussed above, the assumption of a cumulative broadening comes from the general phenomenology of an increasing linewidth of the phonon replicas with the overtone index [13–15]. This effect points out the electron-phonon coupling as the broadening mechanism since the phonon-assisted broadening increases with the order of the electron-phonon interaction process.

Following Ref. [19], we conclude that the phonon-assisted broadening in hBN results in a Gaussian line, which is another indication for the very efficient coupling to phonons in this material, in addition to the fact that the emission spectrum in the deep ultraviolet is fully governed by phonon-assisted recombination.

III. RAMAN SCATTERING SPECTROSCOPY

The quantitative interpretation of the phonon-assisted emission spectrum in hBN (Fig. 1) is obtained with an energy Δ of 6.8 ± 0.5 meV. The ± 0.5 meV uncertainty in the fit is small compared to the 4 meV-FWHM of the narrow $n = 0$ components at 5.765 and 5.795 eV. Nevertheless, with an average value of 6.8 meV, only the lower bound of our estimation interval appears consistent with the typical energy of 6.3 meV found in the literature for the Raman-active E_{2g} mode of low energy [21–24]. However, the latter 6.3 meV energy was measured at room temperature whereas our study focuses on the phonon-assisted emission spectrum in hBN at 10 K. In the prospect of further supporting our demonstration of the existence of overtones of interlayer shear modes in the phonon replicas spectrum, we have performed temperature-dependent Raman experiments in order to obtain the temperature variation of the E_{2g} mode energy and compare it with our estimation of $\Delta = 6.8 \pm 0.5$ meV.

A. Experiments

The Raman scattering measurements were carried out in back-scattering configuration from the c face, using the 514.5-nm line of an Ar+ laser. The scattered light was analyzed using a Jobin-Yvon T64000 triple spectrometer equipped with a liquid nitrogen (LN_2)-cooled CCD detector. The Raman spectra were obtained in the subtractive configuration of the spectrometer with 100-μm slits, which corresponds to a spectral bandwidth of about 2.2 cm^{-1}. The laser power on the sample was kept very low, at 8 mW with a spot size of about 230 μm, in order to avoid heating effects. The sample was mounted in a TBT-Air Liquide LN_2 cryostat equipped with a platinum resistance sensor and a temperature controller. For the high temperature measurements (above 300 K), a Linkam THMS600 heating stage was employed.

B. Results

In Fig. 5, we display in red dots our measurements of the energy of the Raman-active E_{2g} mode of low frequency as a function of temperature, between 77 K and 600 K (more details on the temperature dependence of the Raman modes and the anharmonicity in hBN can be found in Ref. [8]). We observe a monotonous, quasilinear decrease with temperature from 6.6 meV at 77 K to 6.1 meV at 600 K, reflecting the increase of the interlayer spacing due to the positive thermal expansion coefficient along the c axis [8]. At room temperature, we find the energy of 6.35 meV, also reported in Refs. [21–24]. A linear extrapolation of the E_{2g} mode energy at 10 K gives a value of 6.65 meV, which is in excellent agreement with our estimation of $\Delta = 6.8 \pm 0.5$ meV (blue square in Fig. 5). The temperature variation of the Raman-active mode energy displayed in Fig. 5 thus further supports our interpretation of the emission spectrum in hBN, as being governed by phonon-assisted recombination processes involving overtones of low-energy interlayer shear modes.

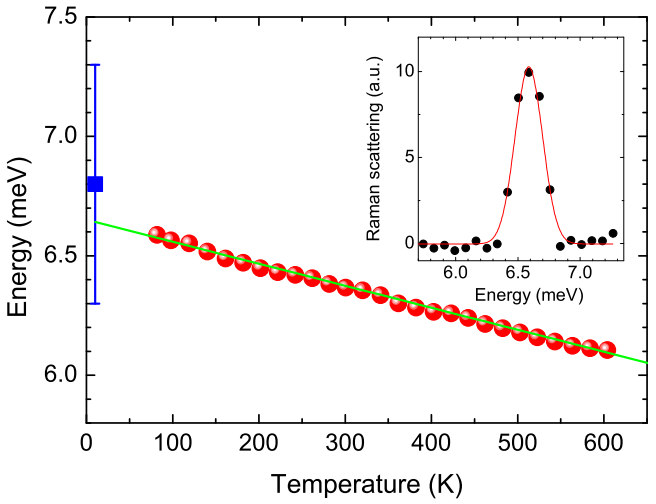

FIG. 5. Temperature dependence of the low-energy Raman-active interlayer shear mode energy between 77 K and 600 K (red dots), and value (blue square) of the energy $\Delta = 6.8 \pm 0.5$ meV estimated from the fit displayed in Fig. 1. Inset: Raman scattering spectrum in bulk hBN, at 80 K.

IV. CONCLUSION

In conclusion, we have brought evidence of overtones of interlayer shear modes in the phonon-assisted emission spectrum in hBN. These lattice vibrations are specific to layered compounds since they correspond to the shear rigid motion between adjacent layers, with a characteristic energy of about 6.8 ± 0.5 meV in hBN at 10 K. We have also demonstrated that the differences observed for the various phonon replicas in hBN only come from the variations of the phonon group velocity at T points of the Brillouin zone. Our quantitative interpretation is based on calculations of the phonon energy and group velocity at T points of the Brillouin zone for each phonon branch. An excellent fit of the multiplet observed in each phonon replica is obtained under the assumption of a cumulative broadening as a function of the overtone index, and with a phenomenological line broadening taken identical for all phonon types. The identification of overtones of interlayer shear modes is further supported by temperature-dependent Raman measurements of the low-energy Raman-active interlayer shear mode in hBN. We point out the need for a microscopic description of the efficient electron-phonon coupling in hBN, which governs the optoelectronic properties of this material, and in particular its bright phonon-assisted emission despite the indirect nature of the band gap.

ACKNOWLEDGMENTS

We gratefully acknowledge C. L'Henoret for his technical support at the mechanics workshop. This work and the PhD funding of T. Q. P. Vuong were financially supported by the network GaNeX (ANR-11-LABX-0014). GaNeX belongs to the publicly funded *Investissements d'Avenir* program managed by the French ANR agency. G.C. is a member of 'Institut Universitaire de France.' This work was also supported by the Spanish MINECO under contract MAT2015-71305-R.

[1] X. F. Jiang, Q. Weng, X. B. Wang, X. Li, J. Zhang, D. Golberg, and Y. Band, J. Mater. Sci. Technol. **31**, 589 (2015).
[2] A. K. Geim and I. V. Grigorieva, Nature (London) **499**, 419 (2013).
[3] M. L. Cohen and A. Zettl, Phys. Today **63**, 34 (2010).
[4] G. Cassabois, P. Valvin, and B. Gil, Nat. Photon. **10**, 262 (2016).
[5] R. J. Elliott, Phys. Rev. **108**, 1384 (1957).
[6] G. Cassabois, P. Valvin, and B. Gil, Phys. Rev. B **93**, 035207 (2016).
[7] J. Serrano, A. Bosak, R. Arenal, M. Krisch, K. Watanabe, T. Taniguchi, H. Kanda, A. Rubio, and L. Wirtz, Phys. Rev. Lett. **98**, 095503 (2007).
[8] R. Cuscó, B. Gil, G. Cassabois, and L. Artús, Phys. Rev. B **94**, 155435 (2016).
[9] T. Q. P. Vuong, G. Cassabois, P. Valvin, V. Jacques, A. Van Der Lee, A. Zobelli, K. Watanabe, T. Taniguchi, and B. Gil, 2D Mater. **4**, 011004 (2017).
[10] B. Segall and G. D. Mahan, Phys. Rev. **171**, 935 (1968).
[11] S. J. Xu, G. Q. Li, S.-J. Xiong, and C. M. Che, J. Appl. Phys. **99**, 073508 (2006).
[12] F. Bassani and G. Pastori Parravicini, *Electronic States and Optical Transitions in Solids* (Pergamon Press, Oxford, New York, 1975).
[13] B. Schreder, C. Dem, M. Schmitt, A. Materny, W. Kiefer, U. Winkler, and E. Umbach, J. Raman Spectrosc. **34**, 100 (2003).
[14] S. Sahoo, V. Sivasubramanian, S. Dhara, and A. K. Arora, Solid State Commun. **147**, 271 (2008).
[15] B. Krummheuer, V. M. Axt, and T. Kuhn, Phys. Rev. B **65**, 195313 (2002).
[16] M. Zacharias, C. E. Patrick, and F. Giustino, Phys. Rev. Lett. **115**, 177401 (2015).
[17] A. Berthelot, I. Favero, G. Cassabois, C. Voisin, C. Delalande, Ph. Roussignol, R. Ferreira, and J. M. Gérard, Nat. Phys. **2**, 759 (2006).
[18] R. Kubo, in *Fluctuation, Relaxation and Resonance in Magnetic Systems*, edited by D. Ter Haar (Oliver and Boyd, Edinburgh, 1962), pp. 23–68.
[19] Y. Toyozawa, Prog. Theor. Phys. **20**, 53 (1958).
[20] L. Schué, B. Berini, A. C. Betz, B. Plaçais, F. Ducastelle, J. Barjon, and A. Loiseau, Nanoscale **8**, 6986 (2016).
[21] R. Geick, C. Perry, and G. Rupprecht, Phys. Rev. **146**, 543 (1966).
[22] T. Kuzuba, K. Era, T. Ishii, and T. Sato, Solid State Commun. **25**, 863 (1978).
[23] R. Nemanich, S. Solin, and R. Martin, Phys. Rev. B **23**, 6348 (1981).
[24] G. Kern, G. Kresse, and J. Hafner, Phys. Rev. B **59**, 8551 (1999).